Naval Research Laboratory
Washington, DC 20375-5000

NRL Memorandum Report 6544

Flux-Corrected Transport Algorithms for Two-Dimensional Compressible Magnetohydrodynamics

C.R. DEVORE

Center for Computational Physics Development
Laboratory for Computational Physics and Fluid Dynamics

September 7, 1989

SECURITY CLASSIFICATION OF THIS PAGE

REPORT DOCUMENTATION PAGE

Form Approved
OMB No. 0704-0188

1a. REPORT SECURITY CLASSIFICATION UNCLASSIFIED	1b. RESTRICTIVE MARKINGS
2a. SECURITY CLASSIFICATION AUTHORITY	3. DISTRIBUTION/AVAILABILITY OF REPORT Approved for public release; distribution unlimited.
2b. DECLASSIFICATION/DOWNGRADING SCHEDULE	
4. PERFORMING ORGANIZATION REPORT NUMBER(S) NRL Memorandum Report 6544	5. MONITORING ORGANIZATION REPORT NUMBER(S)
6a. NAME OF PERFORMING ORGANIZATION Naval Research Laboratory 6b. OFFICE SYMBOL (If applicable) Code 4440	7a. NAME OF MONITORING ORGANIZATION
6c. ADDRESS (City, State, and ZIP Code) Washington, DC 20375-5000	7b. ADDRESS (City, State, and ZIP Code)
8a. NAME OF FUNDING/SPONSORING ORGANIZATION Office of Naval Research 8b. OFFICE SYMBOL (If applicable)	9. PROCUREMENT INSTRUMENT IDENTIFICATION NUMBER
8c. ADDRESS (City, State, and ZIP Code) Arlington, VA 22217	10. SOURCE OF FUNDING NUMBERS PROGRAM ELEMENT NO. 61153N; PROJECT NO.; TASK NO.; WORK UNIT ACCESSION NO. DN280-068
11. TITLE (Include Security Classification) Flux-Corrected Transport Algorithms for Two-Dimensional Compressible Magnetohydrodynamics	
12. PERSONAL AUTHOR(S) DeVore, C.R.	
13a. TYPE OF REPORT Interim 13b. TIME COVERED FROM 1/87 TO 6/89	14. DATE OF REPORT (Year, Month, Day) 1989 September 7 15. PAGE COUNT 25
16. SUPPLEMENTARY NOTATION	

17. COSATI CODES			18. SUBJECT TERMS (Continue on reverse if necessary and identify by block number)
FIELD	GROUP	SUB-GROUP	Finite-difference methods Magnetohydrodynamics

19. ABSTRACT (Continue on reverse if necessary and identify by block number)

Flux-corrected transport (FCT) algorithms for conservatively integrating generalized continuity and hydromagnetic equations in two spatial dimensions are described. By placing the magnetic-field components at the interface locations of the finite-difference grid, the field is kept divergence-free to within machine roundoff error. The new algorithms are particularly well suited for magnetohydrodynamical problems involving shocks and other discontinuities.

20. DISTRIBUTION/AVAILABILITY OF ABSTRACT ☒ UNCLASSIFIED/UNLIMITED ☐ SAME AS RPT ☐ DTIC USERS	21. ABSTRACT SECURITY CLASSIFICATION UNCLASSIFIED
22a. NAME OF RESPONSIBLE INDIVIDUAL C. Richard DeVore	22b. TELEPHONE (Include Area Code) (202) 767-3196 22c. OFFICE SYMBOL Code 4440

DD Form 1473, JUN 86 *Previous editions are obsolete.* SECURITY CLASSIFICATION OF THIS PAGE

S/N 0102-LF-014-6603

CONTENTS

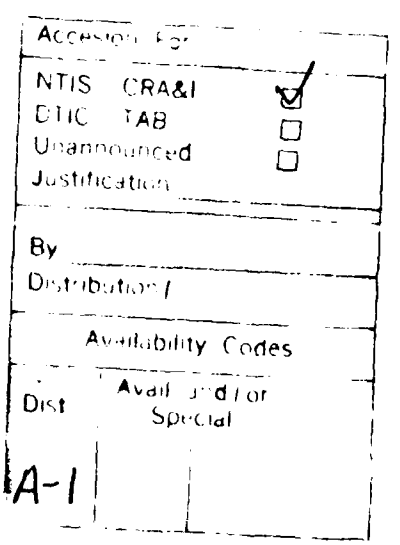

FLUX–CORRECTED TRANSPORT ALGORITHMS FOR TWO–DIMENSIONAL COMPRESSIBLE MAGNETOHYDRODYNAMICS

1. INTRODUCTION

Flux–corrected transport (FCT) [1–9] was originally conceived, and has been developed over the years, as a method for accurately solving the conservation equations of Eulerian hydrodynamics without violating the positivity of mass and energy, particularly near shocks and other discontinuities. This is achieved by adding to the equations a strong numerical diffusion, which guarantees the positivity of the solution, followed by a compensating antidiffusion, which reduces the numerical error. The crux of the FCT method lies in limiting ('correcting') the antidiffusive fluxes before they are applied, so that no unphysical extrema are created in the solution. The effect of this flux–correction procedure is to provide as accurate a solution to the original equation as is consistent with maintaining positivity and monotonicity everywhere.

Recently, a prescription was given [10] for integrating the hydromagnetic equation of magnetohydrodynamics (MHD) using FCT techniques. The discrete values of the magnetic–field components are placed at the interface locations of the finite–difference grid. In this way, the divergence–free character of the magnetic field, as expressed by the discrete integral form of Gauss's law, is simply and strictly preserved. It was shown that the monotonicity constraint of FCT, on the other hand, cannot be strictly enforced without producing an excessively diffuse solution for the magnetic field. A flux–corrector was described which constructs the total antidiffusive flux as the sum of corrected partial fluxes. Each component of the magnetic field contributes a partial flux to the total, and its contribution is limited independently of those due to the other field components. The solution so obtained has remained well behaved even in severe numerical test cases.

In this report, a pair of efficient, accurate algorithms for integrating generalized continuity and hydromagnetic equations in two spatial dimensions will be described. The low–order, diffusive schemes of both the fluid and field solvers have phase and amplitude errors that are second order in the grid spacing at long wavelengths, and are absolutely stable for Courant numbers less than $\frac{1}{2}$. The errors in the high–order, dispersive schemes are fourth order. Several numerical examples will be presented and discussed.

Manuscript approved July 7, 1989.

2. ALGORITHMS

Geometry and Conservation Properties

The conservation equations of Eulerian magnetohydrodynamics take the general form

$$\begin{aligned} \frac{\partial \rho}{\partial t} + \nabla \cdot (\rho \mathbf{v}) &= s_1 + \mathbf{s}_2 \cdot \nabla s_3 + \nabla \cdot \mathbf{s}_4, \\ \frac{\partial \mathbf{B}}{\partial t} &= \nabla \times (\mathbf{v} \times \mathbf{B}) + \nabla \times \mathbf{s}_5, \end{aligned} \tag{1}$$

where ρ is a fluid variable (mass, momentum, or energy density) being time–advanced, $\mathbf{v}$ is the fluid velocity, $\mathbf{B}$ is the magnetic field, and s_1, $\mathbf{s}_2$, s_3, $\mathbf{s}_4$, and $\mathbf{s}_5$ are source terms. In the absence of sources, Eqs. (1) reduce to the continuity and ideal hydromagnetic equations,

$$\begin{aligned} \frac{\partial \rho}{\partial t} + \nabla \cdot (\rho \mathbf{v}) &= 0, \\ \frac{\partial \mathbf{B}}{\partial t} &= \nabla \times (\mathbf{v} \times \mathbf{B}). \end{aligned} \tag{2}$$

The integral conservation relations corresponding to Eqs. (2) are

$$\begin{aligned} \frac{\partial}{\partial t} \int_V \rho dV &= - \oint_S \rho \mathbf{v} \cdot d\mathbf{S}, \\ \frac{\partial}{\partial t} \int_S \mathbf{B} \cdot d\mathbf{S} &= \oint_C \mathbf{v} \times \mathbf{B} \cdot d\mathbf{l}, \end{aligned} \tag{3}$$

where in the first integral V is any volume of fluid bounded by the closed surface S, and in the second S is any (open) surface bounded by the closed contour C.

The geometry of a finite–difference representation of Eqs. (1) is shown in Fig. 1. It has long been recognized that the continuity equation can be integrated conservatively by evaluating the flux densities $\rho \mathbf{v}$ at the interfaces of the spatial grid and using a discrete representation of the integral relation (3a). For example, a forward differencing of the time derivative and an explicit treatment of the spatial derivatives in a two–dimensional problem lead to

$$\begin{aligned} ([\rho^c - \rho^o]\, V)_{ij}\, \Delta t^{-1} = {} & (\rho^o v_x A_x)_{i-\frac{1}{2}j} - (\rho^o v_x A_x)_{i+\frac{1}{2}j} \\ & + (\rho^o v_y A_y)_{ij-\frac{1}{2}} - (\rho^o v_y A_y)_{ij+\frac{1}{2}}, \end{aligned} \tag{4}$$

where ρ^o and ρ^c are the values of the fluid variable before and after the convection, respectively, A_x and A_y are the areas of interfaces normal to the x and y directions, and Δt is the time increment. In a summation of the results (4) over any collection of cells in the system, the contributions of fluxes evaluated at the common, internal interfaces cancel pairwise. The integral conservation relation (3a) in its discrete form then holds for every subvolume of the system.

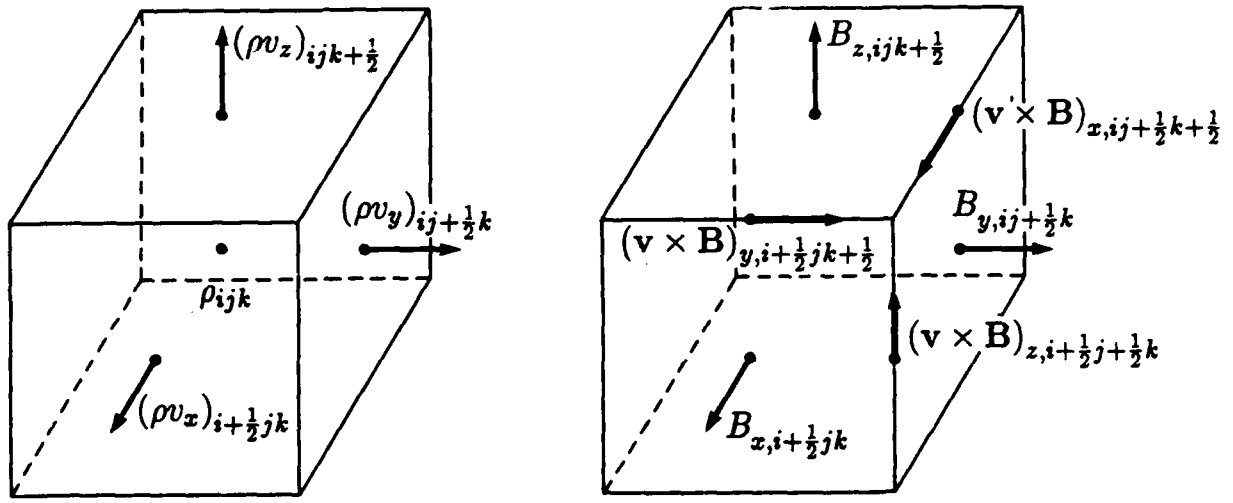

Figure 1. Geometry of the finite–difference representations of the generalized continuity equations (left panel) and hydromagnetic equation (right panel) of conservative, Eulerian magnetohydrodynamics.

(3a) in its discrete form then holds for every subvolume of the system. This result also is true of the generalized continuity equation (1a), if only conservative sources $\mathbf{s}_4$ are present.

A conservative integration of the hydromagnetic equation is similarly effected [11,12] by placing the components of the magnetic field at the cell interfaces, as shown in the right panel of Fig. 1. The flux densities $\mathbf{v}\times\mathbf{B}$ are evaluated at the cell edges, and a discrete representation of the integral conservation relation (3b) again is used. If v_z and B_z both vanish, discretizing in time as before yields

$$\begin{aligned}
\left(\left[B_x^c - B_x^o\right] A_x\right)_{i+\frac{1}{2}j}\,\Delta t^{-1} &= \left(\left[v_y B_x^o - v_x B_y^o\right] L_z\right)_{i+\frac{1}{2}j-\frac{1}{2}} \\
&\quad - \left(\left[v_y B_x^o - v_x B_y^o\right] L_z\right)_{i+\frac{1}{2}j+\frac{1}{2}}, \\
\left(\left[B_y^c - B_y^o\right] A_y\right)_{ij+\frac{1}{2}}\,\Delta t^{-1} &= \left(\left[v_x B_y^o - v_y B_x^o\right] L_z\right)_{i-\frac{1}{2}j+\frac{1}{2}} \\
&\quad - \left(\left[v_x B_y^o - v_y B_x^o\right] L_z\right)_{i+\frac{1}{2}j+\frac{1}{2}},
\end{aligned} \tag{5}$$

where $\mathbf{B}^o$ and $\mathbf{B}^c$ are the field values before and after the convection, and L_z is the length of an edge oriented in the z direction. Due to the pairwise cancellation of fluxes at common edges, the integral relation (3b) in its discrete form holds for any surface in the system. This result is also true of the generalized hydromagnetic equation (1b), whose conservative source term $\mathbf{s}_5$ is likewise evaluated at the cell edges. For the special case of a closed surface, all of the edge fluxes cancel and the solutions obey the discrete equivalent of

$$\frac{\partial}{\partial t}\oint_S \mathbf{B}\cdot d\mathbf{S} = 0. \tag{6}$$

Consequently, if Gauss's law in its discrete integral form is satisfied by the field configuration initially, it is satisfied for all time.

Thus, the conservation properties of both the generalized continuity and hydromagnetic equations (1) can be simply and strictly imposed on their discrete solutions by a judicious choice of the finite–difference representation used to solve them. A pair of algorithms exploiting this representation in two spatial dimensions have been developed, and will be described in the remainder of this section.

Solution of Generalized Continuity Equations

The algorithm for continuity equations is the natural extension to two dimensions of the one–dimensional, low–phase–error algorithm *ETBFCT* [4,6]. Guirguis [7] previously attempted such a generalization, but his scheme suffered from excessive diffusion. The key innovation introduced here is the inclusion of nonvanishing off–diagonal terms in the antidiffusion tensor. Those terms allow the phase and amplitude errors in the high–order solution to be reduced simultaneously to fourth order in the mesh spacing. If only the diagonal terms are nonvanishing, at least one of the errors must increase to second order, as in Guirguis' two–dimensional scheme.

All of these earlier algorithms, and the new one as well, are one–level schemes, whose errors thus are first order in the timestep. To achieve second–order accuracy in time, a predictor/corrector integration is carried out using the one–level scheme for both the half and whole timesteps. Zalesak [5] instead used a two–level, leapfrog–trapezoidal scheme whose errors are second order in time and fourth order in space, and thus is comparable in accuracy to the new algorithm presented here.

The integration schemes consist of convection, diffusion, flux–correction, and antidiffusion stages. For the continuity equation, two intermediate solutions convected solely along x and y, respectively, are needed in addition to the solution convected in both directions, viz.,

$$\begin{aligned}
\rho^{cx}_{ij} V^o_{ij} &= \rho^o_{ij} V^o_{ij} + F^c_{i-\frac{1}{2}j} - F^c_{i+\frac{1}{2}j}, \\
\rho^{cy}_{ij} V^o_{ij} &= \rho^o_{ij} V^o_{ij} + F^c_{ij-\frac{1}{2}} - F^c_{ij+\frac{1}{2}}, \\
\rho^c_{ij} V^o_{ij} &= \rho^o_{ij} V^o_{ij} + F^c_{i-\frac{1}{2}j} - F^c_{i+\frac{1}{2}j} + F^c_{ij-\frac{1}{2}} - F^c_{ij+\frac{1}{2}},
\end{aligned} \tag{7}$$

where V^o_{ij} is the initial cell volume. The convective fluxes along x are given by

$$F^c_{i+\frac{1}{2}j} = \rho^o_{i+\frac{1}{2}j} A^c_{x\, i+\frac{1}{2}j} u_{x\, i+\frac{1}{2}j} \Delta t, \tag{8}$$

in which the interface fluid density is calculated as the average

$$\rho^o_{i+\frac{1}{2}j} = \frac{1}{2}\left(\rho^o_{ij} + \rho^o_{i+1j}\right)$$

and the velocity of the fluid with respect to the moving grid is, in cartesian coordinates,

$$u_{x\,i+\frac{1}{2}j} = v_{x\,i+\frac{1}{2}j} - \Delta t^{-1}\left(x^f_{i+\frac{1}{2}} - x^o_{i+\frac{1}{2}}\right).$$

Here, $x^o_{i+\frac{1}{2}}$ and $x^f_{i+\frac{1}{2}}$ are the initial and final positions, respectively, of the $i+\frac{1}{2}$th interface along x. The interface areas $A^c_{x\,i+\frac{1}{2}j}$ are time– and space–centered, and can be chosen to preserve a uniform field ρ under an arbitrary grid rezoning with zero fluid flow [4,6]. The choice

$$A^c_{x\,i+\frac{1}{2}j} = \frac{1}{2}\left(\Delta y^o_j + \Delta y^f_j\right),$$

where

$$\Delta y^{o,f}_j = y^{o,f}_{j+\frac{1}{2}} - y^{o,f}_{j-\frac{1}{2}},$$

satisfies this requirement. Analogous expressions are used to calculate the y convective fluxes.

The diffusion stage includes the compression due to grid motion and ensures the positivity of the low–order solution,

$$\rho^d_{ij}V^f_{ij} = \rho^c_{ij}V^o_{ij} + F^d_{i-\frac{1}{2}j} - F^d_{i+\frac{1}{2}j} + F^d_{ij-\frac{1}{2}} - F^d_{ij+\frac{1}{2}}, \tag{9}$$

where V^f_{ij} is the final cell volume. The diffusive fluxes along x are calculated from

$$F^d_{i+\frac{1}{2}j} = \nu_{xx\,i+\frac{1}{2}j}\left(\rho^o_{ij} - \rho^o_{i+1j}\right)V^f_{i+\frac{1}{2}j}, \tag{10}$$

in which the diffusion coefficient is

$$\nu_{xx\,i+\frac{1}{2}j} = \frac{1}{6} + \frac{1}{3}\epsilon^2_{x\,i+\frac{1}{2}j}, \tag{11}$$

the signed Courant number for the fluid motion along x is

$$\epsilon_{x\,i+\frac{1}{2}j} = \frac{1}{2}\left(\frac{1}{V^f_{ij}} + \frac{1}{V^f_{i+1j}}\right)u_{x\,i+\frac{1}{2}j}\,A^c_{x\,i+\frac{1}{2}j}\,\Delta t,$$

and the interface volume is

$$V^f_{i+\frac{1}{2}j} = \frac{1}{2}\left(V^f_{ij} + V^f_{i+1j}\right).$$

Adding the contributions of the source terms completes the calculation of the low–order solution,

$$\begin{aligned}\rho^l_{ij}V^f_{ij} = \rho^d_{ij}V^f_{ij} &+ \Delta t\, V^o_{ij}\, s_{1\,ij} \\ &+ \Delta t \frac{1}{2}\left(A^c_{x\,i+\frac{1}{2}j} + A^c_{x\,i-\frac{1}{2}j}\right) s_{2\,x\,ij}\left(s_{3\,i+\frac{1}{2}j} - s_{3\,i-\frac{1}{2}j}\right) \\ &+ \Delta t\left(A^c_{x\,i+\frac{1}{2}j}\, s_{4\,x\,i+\frac{1}{2}j} - A^c_{x\,i-\frac{1}{2}j}\, s_{4\,x\,i-\frac{1}{2}j}\right. \\ &\quad \left. + A^c_{y\,ij+\frac{1}{2}}\, s_{4\,y\,ij+\frac{1}{2}} - A^c_{y\,ij-\frac{1}{2}}\, s_{4\,y\,ij-\frac{1}{2}}\right),\end{aligned} \tag{12}$$

in which the gradient of s_3 has been taken along x, for definiteness.

The antidiffusion stage, if performed without flux–correction, would yield the high–order solution,

$$\rho^h_{ij}V^f_{ij} = \rho^l_{ij}V^f_{ij} + F^a_{i-\frac{1}{2}j} - F^a_{i+\frac{1}{2}j} + F^a_{ij-\frac{1}{2}} - F^a_{ij+\frac{1}{2}}. \tag{13}$$

The antidiffusive fluxes along x are given by

$$\begin{aligned}F^a_{i+\frac{1}{2}j} = &\mu_{xx\,i+\frac{1}{2}j}\left(\rho^{cx}_{i+1j} - \rho^{cx}_{ij}\right) V^f_{i+\frac{1}{2}j} \\ &+ \mu_{xy\,i+\frac{1}{2}j}\left(\rho^{cx}_{i+\frac{1}{2}j+\frac{1}{2}} - \rho^{cx}_{i+\frac{1}{2}j-\frac{1}{2}}\right) V^f_{i+\frac{1}{2}j},\end{aligned} \tag{14}$$

and the antidiffusion coefficients are

$$\begin{aligned}\mu_{xx\,i+\frac{1}{2}j} &= \frac{1}{6} - \frac{1}{6}\epsilon^2_{x\,i+\frac{1}{2}j}, \\ \mu_{xy\,i+\frac{1}{2}j} &= -\frac{1}{2}\epsilon_{x\,i+\frac{1}{2}j}\,\epsilon_{y\,i+\frac{1}{2}j}.\end{aligned} \tag{15}$$

The Courant number at the x interface for flow in the y direction is conveniently calculated as the average

$$\epsilon_{y\,i+\frac{1}{2}j} = \frac{1}{4}\left(\epsilon_{y\,ij-\frac{1}{2}} + \epsilon_{y\,i+1j-\frac{1}{2}} + \epsilon_{y\,ij+\frac{1}{2}} + \epsilon_{y\,i+1j+\frac{1}{2}}\right),$$

as is the convected solution at the cell edge,

$$\rho^{cx}_{i+\frac{1}{2}j+\frac{1}{2}} = \frac{1}{4}\left(\rho^{cx}_{ij} + \rho^{cx}_{i+1j} + \rho^{cx}_{ij+1} + \rho^{cx}_{i+1j+1}\right).$$

The cross–derivative terms, those with coefficients μ_{xy} and μ_{yx}, make the key contributions toward reducing the error in the high–order scheme.

In the flux–correction stage, the first step is to establish the allowed extrema of the final solution from the nine–point comparison

$$\rho^{\max}_{ij} = \max\left(\tilde{\rho}_{i-1j-1}, \tilde{\rho}_{ij-1}, \tilde{\rho}_{i+1j-1}, \tilde{\rho}_{i-1j}, \tilde{\rho}_{ij}, \tilde{\rho}_{i+1j}, \tilde{\rho}_{i-1j+1}, \tilde{\rho}_{ij+1}, \tilde{\rho}_{i+1j+1}\right). \tag{16}$$

Here, $\tilde{\rho}_{ij}$ may be ...en to be simply the low–order (monotonic) value

$$\tilde{\rho}_{ij} = \rho^l_{ij},$$

corresponding to the 'strong' flux–corrector originally introduced by Boris and Book [1]. Alternatively, it may taken to be any physically well–motivated upper bound, e.g.,

$$\tilde{\rho}_{ij} = \max\left(\rho^o_{ij}, \rho^l_{ij}\right),$$

as suggested by Zalesak [5]. Analogous expressions are used to establish $\rho^{\min}_{ij}$.

Second, those antidiffusive fluxes that are directed downstream with respect to the local gradient, i.e., which act to smooth the profile rather than steepen it, are cancelled. Thus, set

$$\begin{aligned} F^a_{i+\frac{1}{2}j} = 0 \quad \text{if} \quad & F^a_{i+\frac{1}{2}j}\left(\rho^l_{i+1j} - \rho^l_{ij}\right) < 0 \\ \text{and} \quad & F^a_{i+\frac{1}{2}j}\left(\rho^l_{i+2j} - \rho^l_{i+1j}\right) < 0 \\ \text{or} \quad & F^a_{i+\frac{1}{2}j}\left(\rho^l_{ij} - \rho^l_{i-1j}\right) < 0. \end{aligned} \tag{17}$$

Such fluxes contribute to the formation of dispersive ripples, degrading the quality of the solution.

The third step is the calculation of the total antidiffusive fluxes into and out of each cell,

$$\begin{aligned} P^+_{ij} &= \max\left(F^a_{i-\frac{1}{2}j}, 0\right) - \min\left(F^a_{i+\frac{1}{2}j}, 0\right) + \max\left(F^a_{ij-\frac{1}{2}}, 0\right) - \min\left(F^a_{ij+\frac{1}{2}}, 0\right), \\ P^-_{ij} &= \max\left(F^a_{i+\frac{1}{2}j}, 0\right) - \min\left(F^a_{i-\frac{1}{2}j}, 0\right) + \max\left(F^a_{ij+\frac{1}{2}}, 0\right) - \min\left(F^a_{ij-\frac{1}{2}}, 0\right), \end{aligned} \tag{18}$$

and the maximum allowed fluxes into and out of the cell,

$$\begin{aligned} Q^+_{ij} &= \left(\rho^{\max}_{ij} - \rho^l_{ij}\right) V^f_{ij}, \\ Q^-_{ij} &= \left(\rho^l_{ij} - \rho^{\min}_{ij}\right) V^f_{ij}. \end{aligned} \tag{19}$$

The ratios of these two quantities determine the fractions of the incoming fluxes that can be applied without causing an overshoot or undershoot in the final solution,

$$\begin{aligned} R^+_{ij} &= \min\left(1, Q^+_{ij}/P^+_{ij}\right), \\ R^-_{ij} &= \min\left(1, Q^-_{ij}/P^-_{ij}\right), \end{aligned} \tag{20}$$

respectively.

Fourth, the flux–correction coefficient for each antidiffusive flux is calculated as the minimum fraction which causes neither an overshoot in the cell downstream from the flux nor an undershoot in the cell upstream,

$$C_{i+\frac{1}{2}j} = \begin{cases} \min\left(R^+_{i+1j}, R^-_{ij}\right), & \text{if } F^a_{i+\frac{1}{2}j} \geq 0; \\ \min\left(R^+_{ij}, R^-_{i+1j}\right), & \text{otherwise.} \end{cases} \tag{21}$$

The fifth and last step is to reduce the fluxes by these fractions, i.e.,

$$\tilde{F}^a_{i+\frac{1}{2}j} = C_{i+\frac{1}{2}j} F^a_{i+\frac{1}{2}j}. \tag{22}$$

Applying the corrected fluxes to the low–order solution yields, finally,

$$\rho^f_{ij} V^f_{ij} = \rho^l_{ij} V^f_{ij} + \tilde{F}^a_{i-\frac{1}{2}j} - \tilde{F}^a_{i+\frac{1}{2}j} + \tilde{F}^a_{ij-\frac{1}{2}} - \tilde{F}^a_{ij+\frac{1}{2}}, \tag{23}$$

the desired solution to the generalized continuity equation (1a).

The positivity of the low–order solution ρ^l, combined with the restrictions imposed by the flux–corrector, ensures the positivity of the final solution ρ^f. Eq. (12) for ρ^l_{ij} can be explicitly evaluated in terms of the neighboring values of ρ^o and $\epsilon_{x,y}$. It is then easily established that positivity is guaranteed, in that the coefficient of each of the ρ^o's is nonnegative, for a locally uniform flow field satisfying $|\epsilon_{x,y}| \leq \frac{1}{2}$. In the extreme case of fluid concentrated in and flowing outward from a single cell, i.e., a point blast wave, the limiting value which ensures positivity is considerably smaller, $|\epsilon_{x,y}| \leq \frac{1}{4}(\sqrt{13} - 3) \approx 0.15$.

The accuracy and stability properties of the algorithm are analyzed by specializing to the case of a uniform, cartesian mesh and a uniform velocity field [3]. The exact solution to the continuity equation for a uniform velocity is $\rho(\mathbf{x},t) = \rho(\mathbf{x} - \mathbf{v}t, 0)$. During the time interval Δt, an initial Fourier mode

$$\rho(\mathbf{x},0) = \rho^0_{\mathbf{k}} e^{i\mathbf{k}\cdot\mathbf{x}} \tag{24a}$$

evolves to

$$\rho(\mathbf{x},\Delta t) = \rho^0_{\mathbf{k}} e^{i\mathbf{k}\cdot(\mathbf{x}-\mathbf{v}\Delta t)}. \tag{24b}$$

The exact solution (24b) can be compared with the numerical solutions (12) and (13) obtained when (24a) is used for ρ^o. In the long–wavelength limit $k \to 0$, the phase and amplitude errors are found to be second order in the mesh spacing for the low–order solution (12), and fourth order for the high–order solution (13). The amplification factor for (12) is less than unity for all wavenumbers $\mathbf{k}$, and thus the algorithm is completely stable, for Courant numbers $|\epsilon_{x,y}| < \frac{1}{2}$.

Solution of the Generalized Hydromagnetic Equation

The algorithm for the hydromagnetic equation is similar in many respects to that for continuity equations. Here, intermediate low–order solutions B^{lx}_x and B^{ly}_y, to which only the B_x– and B_y–dependent fluxes contribute, respectively, are needed. These solutions are not divergence–free, but

they are used solely to correct their associated partial antidiffusive fluxes F_z^{ax} and F_z^{ay}. After correction, these partial fluxes are combined to obtain the total corrected antidiffusive flux $\tilde{F}_z^a$. As discussed in greater detail elsewhere [10], a flux–corrector which limits the total antidiffusive flux F_z^a with respect to B_x and B_y simultaneously tends to be very restrictive, producing an inaccurate, diffuse final solution.

In the convection stage, there results

$$\begin{aligned}
B^{cy}_{x\,i+\frac{1}{2}j} A^o_{x\,i+\frac{1}{2}j} &= B^o_{x\,i+\frac{1}{2}j} A^o_{x\,i+\frac{1}{2}j} + F^{cx}_{i+\frac{1}{2}j-\frac{1}{2}} - F^{cx}_{i+\frac{1}{2}j+\frac{1}{2}}, \\
B^{cx}_{y\,ij+\frac{1}{2}} A^o_{y\,ij+\frac{1}{2}} &= B^o_{y\,ij+\frac{1}{2}} A^o_{y\,ij+\frac{1}{2}} + F^{cy}_{i-\frac{1}{2}j+\frac{1}{2}} - F^{cy}_{i+\frac{1}{2}j+\frac{1}{2}}; \\
B^{c}_{x\,i+\frac{1}{2}j} A^o_{x\,i+\frac{1}{2}j} &= B^o_{x\,i+\frac{1}{2}j} A^o_{x\,i+\frac{1}{2}j} - F^{c}_{i+\frac{1}{2}j-\frac{1}{2}} + F^{c}_{i+\frac{1}{2}j+\frac{1}{2}}, \\
B^{c}_{y\,ij+\frac{1}{2}} A^o_{y\,ij+\frac{1}{2}} &= B^o_{y\,ij+\frac{1}{2}} A^o_{y\,ij+\frac{1}{2}} + F^{c}_{i-\frac{1}{2}j+\frac{1}{2}} - F^{c}_{i+\frac{1}{2}j+\frac{1}{2}},
\end{aligned} \tag{25}$$

where $A^o_{x\,i+\frac{1}{2}j}$ and $A^o_{y\,ij+\frac{1}{2}}$ are the initial interface areas. The convective fluxes due to B_x and B_y separately and jointly are given, respectively, by

$$\begin{aligned}
F^{cx}_{i+\frac{1}{2}j+\frac{1}{2}} &= B^o_{x\,i+\frac{1}{2}j+\frac{1}{2}}\, L^c_{x\,i+\frac{1}{2}j+\frac{1}{2}}\, u_{y\,i+\frac{1}{2}j+\frac{1}{2}}\, \Delta t, \\
F^{cy}_{i+\frac{1}{2}j+\frac{1}{2}} &= B^o_{y\,i+\frac{1}{2}j+\frac{1}{2}}\, L^c_{x\,i+\frac{1}{2}j+\frac{1}{2}}\, u_{x\,i+\frac{1}{2}j+\frac{1}{2}}\, \Delta t, \\
F^{c}_{i+\frac{1}{2}j+\frac{1}{2}} &= F^{cy}_{i+\frac{1}{2}j+\frac{1}{2}} - F^{cx}_{i+\frac{1}{2}j+\frac{1}{2}}.
\end{aligned} \tag{26}$$

The edge magnetic fields are calculated as the averages

$$\begin{aligned}
B^o_{x\,i+\frac{1}{2}j+\frac{1}{2}} &= \frac{1}{2}\left(B^o_{x\,i+\frac{1}{2}j} + B^o_{x\,i+\frac{1}{2}j+1}\right), \\
B^o_{y\,i+\frac{1}{2}j+\frac{1}{2}} &= \frac{1}{2}\left(B^o_{y\,ij+\frac{1}{2}} + B^o_{y\,i+1j+\frac{1}{2}}\right),
\end{aligned}$$

and the velocity of the fluid with respect to the moving grid is, in cartesian coordinates,

$$\begin{aligned}
u_{x\,i+\frac{1}{2}j+\frac{1}{2}} &= v_{x\,i+\frac{1}{2}j+\frac{1}{2}} - \Delta t^{-1}\left(x^f_{i+\frac{1}{2}} - x^o_{i+\frac{1}{2}}\right), \\
u_{y\,i+\frac{1}{2}j+\frac{1}{2}} &= v_{y\,i+\frac{1}{2}j+\frac{1}{2}} - \Delta t^{-1}\left(y^f_{j+\frac{1}{2}} - y^o_{j+\frac{1}{2}}\right).
\end{aligned}$$

The edge lengths $L^c_{z\,i+\frac{1}{2}j+\frac{1}{2}}$ are to be time– and space–centered.

The diffusion stage ensures the monotonicity of the low–order solution and includes the compression due to grid motion,

$$\begin{aligned}
B^{dy}_{x\,i+\frac{1}{2}j} A^f_{x\,i+\frac{1}{2}j} &= B^{cy}_{x\,i+\frac{1}{2}j} A^o_{x\,i+\frac{1}{2}j} + F^{dx}_{i+\frac{1}{2}j-\frac{1}{2}} - F^{dx}_{i+\frac{1}{2}j+\frac{1}{2}}, \\
B^{dx}_{y\,ij+\frac{1}{2}} A^f_{y\,ij+\frac{1}{2}} &= B^{cx}_{y\,ij+\frac{1}{2}} A^o_{y\,ij+\frac{1}{2}} + F^{dy}_{i-\frac{1}{2}j+\frac{1}{2}} - F^{dy}_{i+\frac{1}{2}j+\frac{1}{2}}; \\
B^{d}_{x\,i+\frac{1}{2}j} A^f_{x\,i+\frac{1}{2}j} &= B^{c}_{x\,i+\frac{1}{2}j} A^o_{x\,i+\frac{1}{2}j} - F^{d}_{i+\frac{1}{2}j-\frac{1}{2}} + F^{d}_{i+\frac{1}{2}j+\frac{1}{2}}, \\
B^{d}_{y\,ij+\frac{1}{2}} A^f_{y\,ij+\frac{1}{2}} &= B^{c}_{y\,ij+\frac{1}{2}} A^o_{y\,ij+\frac{1}{2}} + F^{d}_{i-\frac{1}{2}j+\frac{1}{2}} - F^{d}_{i+\frac{1}{2}j+\frac{1}{2}}.
\end{aligned} \tag{27}$$

Here, $A^f_{x\,i+\frac{1}{2}j}$ and $A^f_{y\,ij+\frac{1}{2}}$ are the final interface areas. The diffusive fluxes are given by

$$\begin{aligned} F^{dx}_{i+\frac{1}{2}j+\frac{1}{2}} &= \nu_{yy\,i+\frac{1}{2}j+\frac{1}{2}} \left(B^o_{x\,i+\frac{1}{2}j} - B^o_{x\,i+\frac{1}{2}j+1} \right) A^f_{xi+\frac{1}{2}j+\frac{1}{2}}, \\ F^{dy}_{i+\frac{1}{2}j+\frac{1}{2}} &= \nu_{xx\,i+\frac{1}{2}j+\frac{1}{2}} \left(B^o_{y\,ij+\frac{1}{2}} - B^o_{y\,i+1j+\frac{1}{2}} \right) A^f_{yi+\frac{1}{2}j+\frac{1}{2}}, \\ F^d_{i+\frac{1}{2}j+\frac{1}{2}} &= F^{dy}_{i+\frac{1}{2}j+\frac{1}{2}} - F^{dx}_{i+\frac{1}{2}j+\frac{1}{2}}. \end{aligned} \tag{28}$$

For the diffusion along x, the coefficient is

$$\nu_{xx\,i+\frac{1}{2}j+\frac{1}{2}} = \frac{1}{6} + \frac{1}{3}\epsilon^2_{x\,i+\frac{1}{2}j+\frac{1}{2}}, \tag{29}$$

the signed Courant number is

$$\epsilon_{x\,i+\frac{1}{2}j+\frac{1}{2}} = \frac{1}{2}\left(\frac{1}{A^f_{y\,ij+\frac{1}{2}}} + \frac{1}{A^f_{y\,i+1j+\frac{1}{2}}} \right) u_{x\,i+\frac{1}{2}j+\frac{1}{2}}\, L^c_{x\,i+\frac{1}{2}j+\frac{1}{2}}\, \Delta t,$$

and the edge area is the average

$$A^f_{y\,i+\frac{1}{2}j+\frac{1}{2}} = \frac{1}{2}\left(A^f_{y\,ij+\frac{1}{2}} + A^f_{y\,i+1j+\frac{1}{2}} \right).$$

Analogous definitions apply along y. Adding the contributions of the source term yields the low-order solutions,

$$\begin{aligned} B^{lx}_{x\,i+\frac{1}{2}j} A^f_{x\,i+\frac{1}{2}j} &= B^{dy}_{x\,i+\frac{1}{2}j} A^f_{x\,i+\frac{1}{2}j} - F^s_{i+\frac{1}{2}j-\frac{1}{2}} + F^s_{i+\frac{1}{2}j+\frac{1}{2}}, \\ B^{ly}_{y\,ij+\frac{1}{2}} A^f_{y\,ij+\frac{1}{2}} &= B^{dx}_{y\,ij+\frac{1}{2}} A^f_{y\,ij+\frac{1}{2}} + F^s_{i-\frac{1}{2}j+\frac{1}{2}} - F^s_{i+\frac{1}{2}j+\frac{1}{2}}; \\ B^l_{x\,i+\frac{1}{2}j} A^f_{x\,i+\frac{1}{2}j} &= B^d_{x\,i+\frac{1}{2}j} A^f_{x\,i+\frac{1}{2}j} - F^s_{i+\frac{1}{2}j-\frac{1}{2}} + F^s_{i+\frac{1}{2}j+\frac{1}{2}}, \\ B^l_{y\,ij+\frac{1}{2}} A^f_{y\,ij+\frac{1}{2}} &= B^d_{y\,ij+\frac{1}{2}} A^f_{y\,ij+\frac{1}{2}} + F^s_{i-\frac{1}{2}j+\frac{1}{2}} - F^s_{i+\frac{1}{2}j+\frac{1}{2}}, \end{aligned} \tag{30}$$

where

$$F^s_{i+\frac{1}{2}j+\frac{1}{2}} = \Delta t\, L^c_{x\,i+\frac{1}{2}j+\frac{1}{2}} s_{5\,x\,i+\frac{1}{2}j+\frac{1}{2}}$$

is the edge flux due to the source term s_5.

The high-order solutions are given by

$$\begin{aligned} B^h_{x\,i+\frac{1}{2}j} A^f_{x\,i+\frac{1}{2}j} &= B^l_{x\,i+\frac{1}{2}j} A^f_{x\,i+\frac{1}{2}j} - F^a_{i+\frac{1}{2}j-\frac{1}{2}} + F^a_{i+\frac{1}{2}j+\frac{1}{2}}, \\ B^h_{y\,ij+\frac{1}{2}} A^f_{y\,ij+\frac{1}{2}} &= B^l_{y\,ij+\frac{1}{2}} A^f_{y\,ij+\frac{1}{2}} + F^a_{i-\frac{1}{2}j+\frac{1}{2}} - F^a_{i+\frac{1}{2}j+\frac{1}{2}}. \end{aligned} \tag{31}$$

The uncorrected partial and total antidiffusive fluxes are

$$\begin{aligned}
F^{ax}_{i+\frac{1}{2}j+\frac{1}{2}} =& \mu_{yy\,i+\frac{1}{2}j+\frac{1}{2}} \left(B^{cy}_{x\,i+\frac{1}{2}j+1} - B^{cy}_{x\,i+\frac{1}{2}j} \right) A^{f}_{xi+\frac{1}{2}j+\frac{1}{2}} \\
&+ \mu_{yx\,i+\frac{1}{2}j+\frac{1}{2}} \left(B^{cy}_{x\,i+1j+\frac{1}{2}} - B^{cy}_{x\,ij+\frac{1}{2}} \right) A^{f}_{xi+\frac{1}{2}j+\frac{1}{2}}, \\
F^{ay}_{i+\frac{1}{2}j+\frac{1}{2}} =& \mu_{xx\,i+\frac{1}{2}j+\frac{1}{2}} \left(B^{cx}_{y\,i+1j+\frac{1}{2}} - B^{cx}_{y\,ij+\frac{1}{2}} \right) A^{f}_{yi+\frac{1}{2}j+\frac{1}{2}} \\
&+ \mu_{xy\,i+\frac{1}{2}j+\frac{1}{2}} \left(B^{cx}_{y\,i+\frac{1}{2}j+1} - B^{cx}_{y\,i+\frac{1}{2}j} \right) A^{f}_{yi+\frac{1}{2}j+\frac{1}{2}}, \\
F^{a}_{i+\frac{1}{2}j+\frac{1}{2}} =& F^{ay}_{i+\frac{1}{2}j+\frac{1}{2}} - F^{ax}_{i+\frac{1}{2}j+\frac{1}{2}},
\end{aligned} \tag{32}$$

where the coefficients for antidiffusion along x are

$$\begin{aligned}
\mu_{xx\,i+\frac{1}{2}j+\frac{1}{2}} &= \frac{1}{6} - \frac{1}{6}\epsilon^{2}_{x\,i+\frac{1}{2}j+\frac{1}{2}}, \\
\mu_{xy\,i+\frac{1}{2}j+\frac{1}{2}} &= -\frac{1}{2}\epsilon_{x\,i+\frac{1}{2}j+\frac{1}{2}}\,\epsilon_{y\,i+\frac{1}{2}j+\frac{1}{2}}.
\end{aligned} \tag{33}$$

The convected solution for B_x at the y interfaces is calculated as the average

$$B^{cx}_{x\,ij+\frac{1}{2}} = \frac{1}{4}\left(B^{cx}_{x\,i-\frac{1}{2}j} + B^{cx}_{x\,i-\frac{1}{2}j+1} + B^{cx}_{x\,i+\frac{1}{2}j} + B^{cx}_{x\,i+\frac{1}{2}j+1} \right).$$

The coefficients for antidiffusion along y and the convected solution for B_y at the x interfaces are calculated analogously.

In the flux–correction stage, the permitted extremal values of the solutions are calculated from

$$\begin{aligned}
B^{\max}_{x\,i+\frac{1}{2}j} &= \max\left(\tilde{B}_{xi+\frac{1}{2}j-1}, \tilde{B}_{x\,i+\frac{1}{2}j}, \tilde{B}_{x\,i+\frac{1}{2}j+1} \right), \\
B^{\max}_{y\,ij+\frac{1}{2}} &= \max\left(\tilde{B}_{yi-1j+\frac{1}{2}}, \tilde{B}_{y\,ij+\frac{1}{2}}, \tilde{B}_{y\,i+1j+\frac{1}{2}} \right).
\end{aligned} \tag{34}$$

For the strong flux–corrector, set

$$\begin{aligned}
\tilde{B}_{x\,i+\frac{1}{2}j} &= B^{lx}_{x\,i+\frac{1}{2}j}, \\
\tilde{B}_{y\,ij+\frac{1}{2}} &= B^{ly}_{y\,ij+\frac{1}{2}},
\end{aligned}$$

and for the weak flux–corrector,

$$\begin{aligned}
\tilde{B}_{x\,i+\frac{1}{2}j} &= \max\left(B^{o}_{x\,i+\frac{1}{2}j}, B^{lx}_{x\,i+\frac{1}{2}j} \right), \\
\tilde{B}_{y\,ij+\frac{1}{2}} &= \max\left(B^{o}_{y\,ij+\frac{1}{2}}, B^{ly}_{y\,ij+\frac{1}{2}} \right).
\end{aligned}$$

$B^{\min}_{x\,i+\frac{1}{2}j}$ and $B^{\min}_{y\,ij+\frac{1}{2}}$ are calculated similarly.

Those partial antidiffusive fluxes that are directed downstream are cancelled according to

$$\begin{aligned}
F^{ax}_{i+\frac{1}{2}j+\frac{1}{2}} = 0 \quad \text{if} \quad & F^{ax}_{i+\frac{1}{2}j+\frac{1}{2}} \left(B^{lx}_{x\, i+\frac{1}{2}j+1} - B^{lx}_{x\, i+\frac{1}{2}j} \right) < 0 \\
\text{and} \quad & F^{ax}_{i+\frac{1}{2}j+\frac{1}{2}} \left(B^{lx}_{x\, i+\frac{1}{2}j+2} - B^{lx}_{x\, i+\frac{1}{2}j+1} \right) < 0 \\
\text{or} \quad & F^{ax}_{i+\frac{1}{2}j+\frac{1}{2}} \left(B^{lx}_{x\, i+\frac{1}{2}j} - B^{lx}_{x\, i+\frac{1}{2}j-1} \right) < 0, \\
F^{ay}_{i+\frac{1}{2}j+\frac{1}{2}} = 0 \quad \text{if} \quad & F^{ay}_{i+\frac{1}{2}j+\frac{1}{2}} \left(B^{ly}_{y\, i+1j+\frac{1}{2}} - B^{ly}_{y\, ij+\frac{1}{2}} \right) < 0 \\
\text{and} \quad & F^{ay}_{i+\frac{1}{2}j+\frac{1}{2}} \left(B^{ly}_{y\, i+2j+\frac{1}{2}} - B^{ly}_{y\, i+1j+\frac{1}{2}} \right) < 0 \\
\text{or} \quad & F^{ay}_{i+\frac{1}{2}j+\frac{1}{2}} \left(B^{ly}_{y\, ij+\frac{1}{2}} - B^{ly}_{y\, i-1j+\frac{1}{2}} \right) < 0.
\end{aligned} \tag{35}$$

Then, the ratios of the maximum partial antidiffusive fluxes into each interface,

$$\begin{aligned}
P^{+}_{i+\frac{1}{2}j} &= \max\left(F^{ax}_{i+\frac{1}{2}j-\frac{1}{2}}, 0 \right) - \min\left(F^{ax}_{i+\frac{1}{2}j+\frac{1}{2}}, 0 \right), \\
P^{+}_{ij+\frac{1}{2}} &= \max\left(F^{ay}_{i-\frac{1}{2}j+\frac{1}{2}}, 0 \right) - \min\left(F^{ay}_{i+\frac{1}{2}j+\frac{1}{2}}, 0 \right),
\end{aligned} \tag{36}$$

to the maximum allowed fluxes into the interfaces,

$$\begin{aligned}
Q^{+}_{i+\frac{1}{2}j} &= \left(B^{\max}_{x\, i+\frac{1}{2}j} - B^{lx}_{x\, i+\frac{1}{2}j} \right) A^{f}_{x\, i+\frac{1}{2}j}, \\
Q^{+}_{ij+\frac{1}{2}} &= \left(B^{\max}_{y\, ij+\frac{1}{2}} - B^{ly}_{y\, ij+\frac{1}{2}} \right) A^{f}_{y\, ij+\frac{1}{2}},
\end{aligned} \tag{37}$$

determine the fractions of the incoming partial fluxes that can be applied without causing overshoots,

$$\begin{aligned}
R^{+}_{i+\frac{1}{2}j} &= \min\left(1, Q^{+}_{i+\frac{1}{2}j} / P^{+}_{i+\frac{1}{2}j} \right), \\
R^{+}_{ij+\frac{1}{2}} &= \min\left(1, Q^{+}_{ij+\frac{1}{2}} / P^{+}_{ij+\frac{1}{2}} \right).
\end{aligned} \tag{38}$$

The fractions $R^{-}_{i+\frac{1}{2}j}$ and $R^{-}_{ij+\frac{1}{2}}$ of the outgoing fluxes that can be applied without causing undershoots are calculated similarly.

The flux–correction coefficients for the partial antidiffusive fluxes now are determined as the minimum fractions which cause neither overshoots in the interfaces downstream from the fluxes, nor undershoots in the interfaces upstream,

$$\begin{aligned}
C^{x}_{i+\frac{1}{2}j+\frac{1}{2}} &= \begin{cases} \min\left(R^{+}_{i+\frac{1}{2}j+1}, R^{-}_{i+\frac{1}{2}j} \right), & \text{if } F^{ax}_{i+\frac{1}{2}j+\frac{1}{2}} \geq 0; \\ \min\left(R^{+}_{i+\frac{1}{2}j}, R^{-}_{i+\frac{1}{2}j+1} \right), & \text{otherwise;} \end{cases} \\
C^{y}_{i+\frac{1}{2}j+\frac{1}{2}} &= \begin{cases} \min\left(R^{+}_{i+1j+\frac{1}{2}}, R^{-}_{ij+\frac{1}{2}} \right), & \text{if } F^{ay}_{i+\frac{1}{2}j+\frac{1}{2}} \geq 0; \\ \min\left(R^{+}_{ij+\frac{1}{2}}, R^{-}_{i+1j+\frac{1}{2}} \right), & \text{otherwise.} \end{cases}
\end{aligned} \tag{39}$$

Reducing the partial fluxes by these fractions and combining them to obtain the total corrected antidiffusive flux yields

$$\begin{aligned}
\tilde{F}^{ax}_{i+\frac{1}{2}j+\frac{1}{2}} &= C^{x}_{i+\frac{1}{2}j+\frac{1}{2}} F^{ax}_{i+\frac{1}{2}j+\frac{1}{2}}, \\
\tilde{F}^{ay}_{i+\frac{1}{2}j+\frac{1}{2}} &= C^{y}_{i+\frac{1}{2}j+\frac{1}{2}} F^{ay}_{i+\frac{1}{2}j+\frac{1}{2}}, \\
\tilde{F}^{a}_{i+\frac{1}{2}j+\frac{1}{2}} &= \tilde{F}^{ay}_{i+\frac{1}{2}j+\frac{1}{2}} - \tilde{F}^{ax}_{i+\frac{1}{2}j+\frac{1}{2}}.
\end{aligned} \tag{40}$$

Finally, the corrected fluxes are applied to the low–order solutions to get

$$\begin{aligned}
B^{f}_{x\,i+\frac{1}{2}j} A^{f}_{x\,i+\frac{1}{2}j} &= B^{l}_{x\,i+\frac{1}{2}j} A^{f}_{x\,i+\frac{1}{2}j} - \tilde{F}^{a}_{i+\frac{1}{2}j-\frac{1}{2}} + \tilde{F}^{a}_{i+\frac{1}{2}j+\frac{1}{2}}, \\
B^{f}_{y\,ij+\frac{1}{2}} A^{f}_{y\,ij+\frac{1}{2}} &= B^{l}_{y\,ij+\frac{1}{2}} A^{f}_{y\,ij+\frac{1}{2}} + \tilde{F}^{a}_{i-\frac{1}{2}j+\frac{1}{2}} - \tilde{F}^{a}_{i+\frac{1}{2}j+\frac{1}{2}},
\end{aligned} \tag{41}$$

the desired solution to the generalized hydromagnetic equation (1b).

The accuracy and stability properties of this algorithm are identical to those for the algorithm for continuity equations. A key step in the analysis is the elimination of B^{o}_{y} in favor of B^{o}_{x}, which is effected by using the divergence–free constraint. For the Fourier mode

$$\mathbf{B}(\mathbf{x},0) = \mathbf{B}^{0}_{\mathbf{k}} e^{i\mathbf{k}\cdot\mathbf{x}},$$

the discrete form of Gauss's law becomes

$$\frac{\sin\beta_x}{\Delta x} B^{0}_{x\,\mathbf{k}} + \frac{\sin\beta_y}{\Delta y} B^{0}_{y\,\mathbf{k}} = 0,$$

where, e.g., Δx is the mesh spacing along x and $\beta_x = \frac{1}{2} k_x \Delta x$. There results

$$\frac{B^{l,h}_{x\,\mathbf{k}}}{B^{o}_{x\,\mathbf{k}}} = \frac{B^{l,h}_{y\,\mathbf{k}}}{B^{o}_{y\,\mathbf{k}}} = \frac{\rho^{l,h}_{\mathbf{k}}}{\rho^{o}_{\mathbf{k}}},$$

so that the errors in the magnetic field are second order for the low–order solution (30) and fourth order for the high–order solution (31), and the algorithm is completely stable for Courant numbers less than $\frac{1}{2}$.

3. EXAMPLES

The new FCT algorithms described in the previous section have been programmed in single–precision FORTRAN and optimized for use on NRL's Cray X–MP/24. Internal storage in these routines is minimized by stepping through the mesh one line at a time, so that no full, two–dimensional work arrays are required. Consequently, the modules use little more memory than a

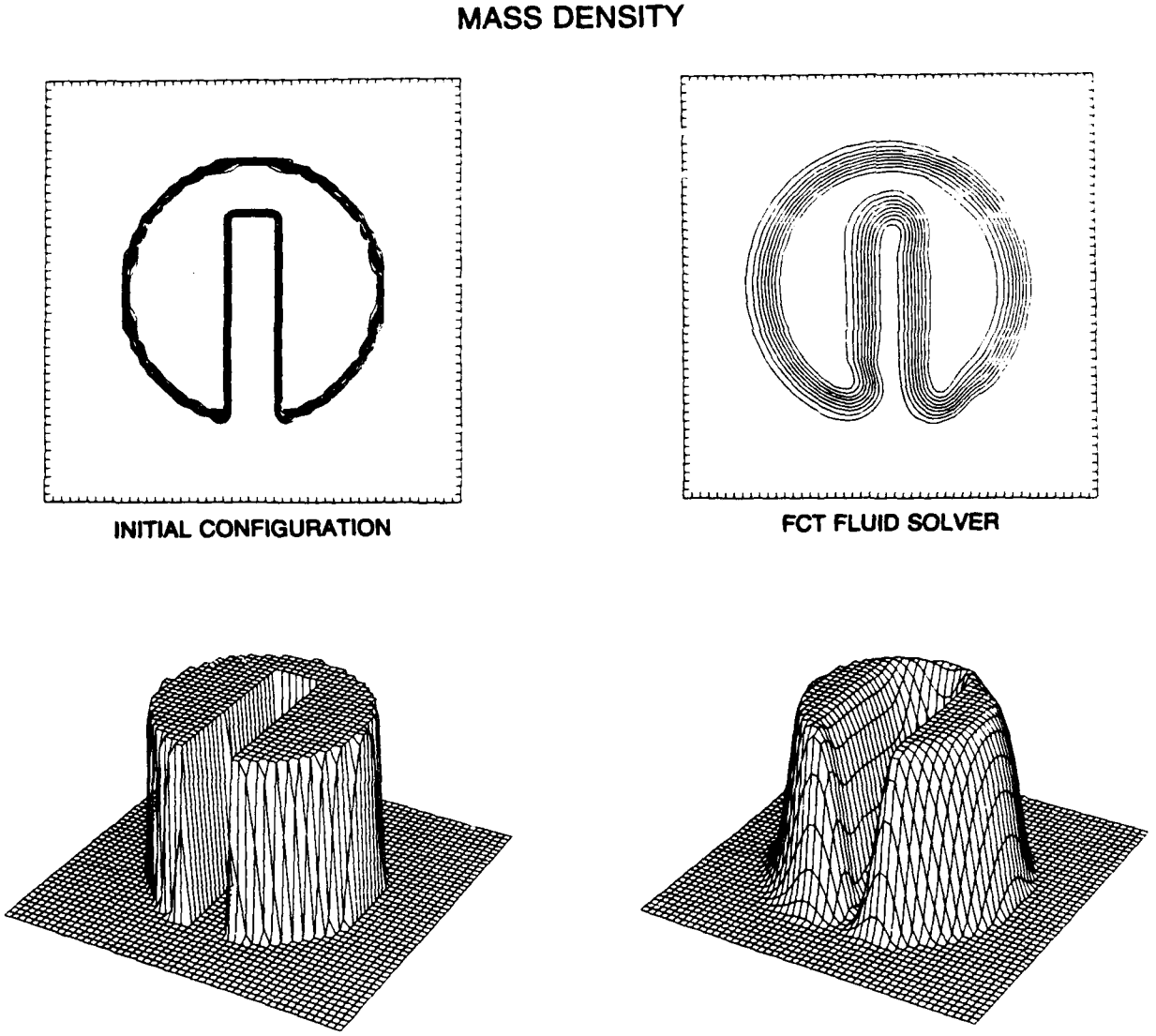

Figure 2. The mass density ρ for a passive advection test is displayed in its initial state (left) and in the final state produced by the new FCT fluid solver (right). Only the 50 × 50 subdomain centered on the slotted cylinder is shown. The axis of rotation is marked by the solid dots in the plots of the initial state. The mass density is contoured at 10%, 20%, ..., 90% of its peak initial value.

corresponding FCT routine for one–dimensional continuity equations. In hydrodynamical advection tests on modest–sized (100 × 100) problems, the multidimensional fluid solver needed only about 10% more time to obtain a solution than did the one–dimensional solver used in operator–split mode (3 μs cell^{-1} timestep^{-1}), and its solution was highly superior (cf. [5,6]).

The new algorithms will be applied here to some kinematical and dynamical problems of hydrodynamics and hydromagnetics. The first test is the rigid rotation of a slotted cylinder, as

calculated with the new fluid solver. Zalesak [5,6] introduced this test to compare operator–split and fully multidimensional solutions for an incompressible flow field. Initial conditions for the calculation are shown in the left panel of Fig. 2. The cylinder rotates rigidly in the counterclockwise direction at an angular rate ω, whence

$$v_x = -\omega y, \qquad v_y = +\omega x,$$

where the origin of the cartesian coordinate system is placed on the axis of rotation. The calculations were performed on a 100 x 100 mesh, with the cylinder initially centered in the upper half plane and its radius set at 15 zones. A slot of width six zones runs through its center, with a bridge of the same width left at the top, joining the two halves of the cylinder. The Courant number is 0.25, so that 1256 timesteps are required for one complete rotation in the plane.

The solution obtained by the FCT fluid solver is shown in the right panel of Fig. 2. The quantitative error in the mass density, calculated from

$$\epsilon = \frac{\sum_{i,j} \left| \rho_{ij}^{\text{analytic}} - \rho_{ij}^{\text{numeric}} \right|}{\sum_{i,j} \left| \rho_{ij}^{\text{analytic}} \right|},$$

is 25%. Both the filling of the slot and the erosion of the bridge are limited to less than 10%. In contrast, an operator–split integration with the one–dimensional routine fills the slot and erodes the bridge by more than 20%. Qualitatively, the multidimensional solution compares very favorably with Zalesak's leapfrog–trapezoidal results, as expected from the similar error properties of the two algorithms.

Turning now to the hydromagnetic tests, a commonly employed alternative to solving directly for the magnetic field in MHD simulations is to use a vector potential representation,

$$\mathbf{B} = \nabla \times \mathbf{A},$$

whence the generalized hydromagnetic equation (1) becomes

$$\frac{\partial \mathbf{A}}{\partial t} = \mathbf{v} \times \nabla \times \mathbf{A} + \mathbf{s}_5.$$

In two dimensions, only the component of the potential along the symmetry direction is needed, and this equation can be reduced to

$$\frac{\partial \psi}{\partial t} + \mathbf{v} \cdot \nabla \psi = \tilde{s}_5, \tag{42}$$

where the flux function ψ is a product of the symmetry component of the potential and a coordinate–system–dependent geometrical factor. The flux function is a convenient primitive variable, because algorithms for generalized continuity equations can be modified to integrate advection equations such as Eq. (42). Also, it is a useful diagnostic since it can be shown that

$$\mathbf{B} \cdot \nabla \psi = 0,$$

i.e., surfaces of constant ψ are magnetic surfaces.

In the remaining examples, direct solutions of the hydromagnetic equation (1) are calculated using the new FCT field solver. They will be compared with indirect solutions obtained by integrating Eq. (42) for the flux function using a modified version of the new FCT fluid solver. The discrete values of ψ are placed at the cell edges $\left(i + \frac{1}{2}, j + \frac{1}{2}\right)$, for consistency between the two calculations. The associated vector potential then is conservatively differenced to yield values of the magnetic–field components at the cell interfaces.

The second test is the rigid rotation of a current–carrying cylinder, analogous to the slotted–cylinder test for the fluid solver. In cartesian coordinates, the flux function and the symmetry component of the vector potential are identical, $\psi = A_z$. Initial conditions for the calculation are shown in the top panel of Fig. 3. The potential, magnetic field, and current density within the cylinder are given by

$$A_z = \frac{r_0 B_0}{2}\left(1 - \frac{r^2}{r_0^2}\right),$$

$$B_\phi = \frac{r}{r_0} B_0,$$

$$J_z = \frac{2B_0}{r_0},$$

where (r, ϕ, z) is a cylindrical coordinate system centered on the cylinder of radius r_0 and peak field strength B_0. A sheath of return current at $r = r_0$ neutralizes the current carried in the interior, so that A_z, B_ϕ, and J_z all vanish for $r > r_0$. The other parameters of the calculation are the same as for the test of the fluid solver.

Figure 3. [*Facing page*] The vector potential A_z (left) and current density J_z (right) for a passive advection test are displayed in their initial state (top) and in the final states produced by the new FCT solvers for the magnetic field (middle) and vector potential (bottom). Only the 50 × 50 subdomain centered on the cylinder is shown. The axis of rotation is marked by the solid dots in the plots of the initial state. The vector potential is contoured at 10%, 20%, ..., 90% of its peak initial value. The current density is contoured at ± 10%, ± 30%, ..., ± 90% of its initial interior value, with positive (negative) percentages represented by the solid (dashed) lines.

VECTOR POTENTIAL

CURRENT DENSITY

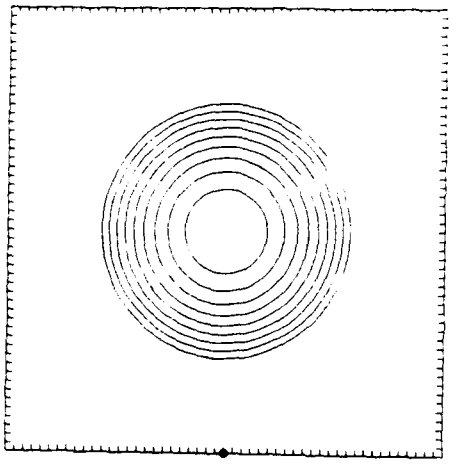

INITIAL CONFIGURATION

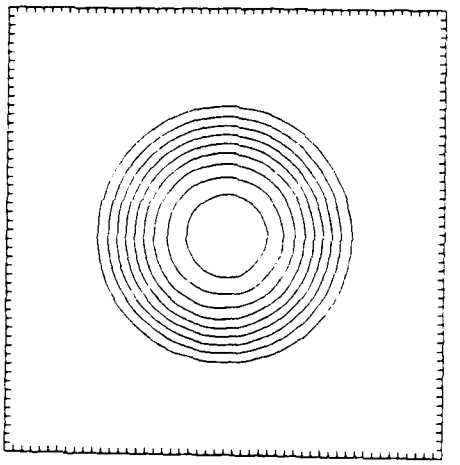

FCT FIELD SOLVER

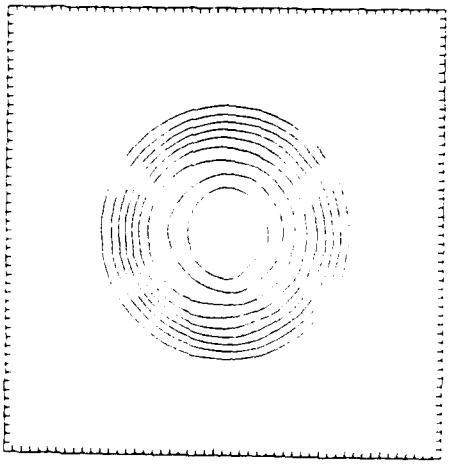

FCT POTENTIAL SOLVER

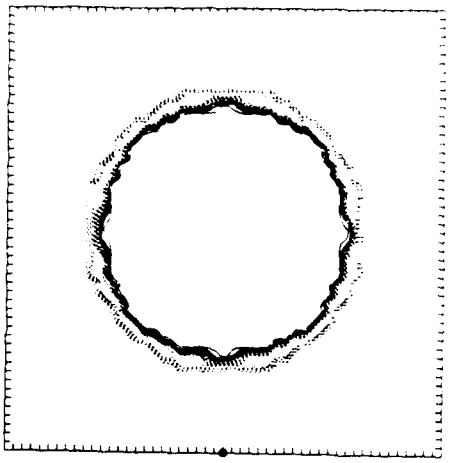

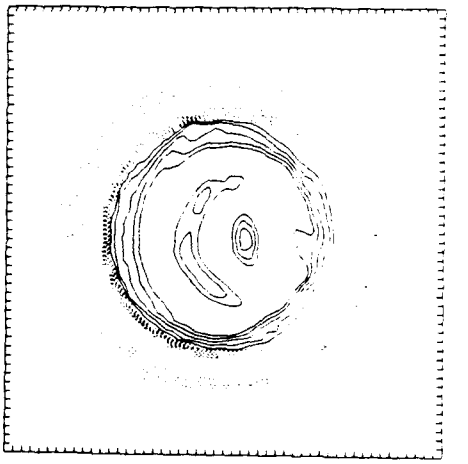

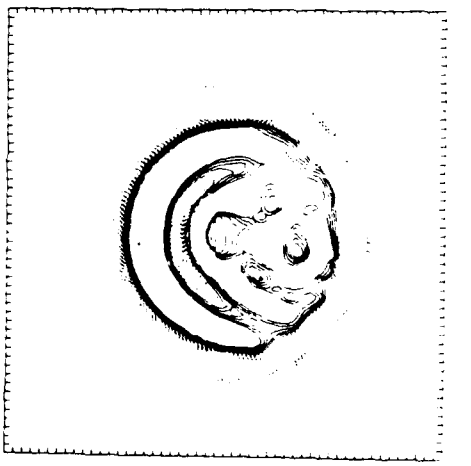

The solutions obtained by the FCT field and potential solvers are shown in the middle and bottom panels, respectively, of Fig. 3. The errors in the vector potentials are very small in both cases, 6% for the field solver and 4% for the potential solver. Although the field solver clearly preserves the symmetry of the flux surfaces better, yielding the better qualitative appearance, its solution is somewhat more diffuse, which accounts for its lower quantitative accuracy. The errors in the magnetic fields are essentially identical for the two solvers, at 25%, and are the same as obtained in the similar hydrodynamical test. For the field solver, this error reflects the difficulty in advecting a discontinuous function (the magnetic field at $r = r_0$) using an Eulerian difference method. For the potential solver, on the other hand, the error reflects the inaccuracies in the numerical derivatives of a smooth function (the vector potential) which has been accurately time-advanced by a monotonic scheme. The latter error is further amplified in the higher derivatives, sufficiently so that the potential solver yields a current density that is less accurate than does the field solver, by 90% to 79%. While both solutions for the current density show local depressions inside the cylinder, the potential solver produces the more severe fluctuations, including a reversal near the axis of symmetry whose amplitude exceeds 70%. The solution provided by the field solver is both qualitatively and quantitatively superior, although it again suffers in the error comparison because its profile is not as sharp.

The third test is the self-similar spherical expansion of a strong shock wave and trailing magnetic bubble out of the gravitational well of a star [13,14]. In this dynamical problem, the self-similar character of the expansion is maintained by a balance between pressure and magnetic forces in the colatitudinal direction and between pressure, magnetic, gravitational, and inertial forces in the radial direction. The simplest expansion is an inertial flow, whence

$$v_r(r,\theta,t) = \frac{r}{t}.$$

At time t_0, the shock and its associated contact surface coincide at radius r_0; at later times, their positions are given by

$$\frac{r_s(t)}{r_0} = \left(\frac{t}{t_0}\right)^{\frac{7}{6}},$$

$$\frac{r_c(t)}{r_0} = \left(\frac{t}{t_0}\right),$$

respectively. A magnetic bubble is embedded behind the contact surface, and the flux function $\psi = r\sin\theta A_\phi$ initially satisfies

$$\psi(r,\theta,t_0) = \begin{cases} \psi_0 (r_2 - r)(r - r_1)\sin^2\theta, & \text{if } r_1 < r < r_2; \\ 0, & \text{otherwise,} \end{cases}$$

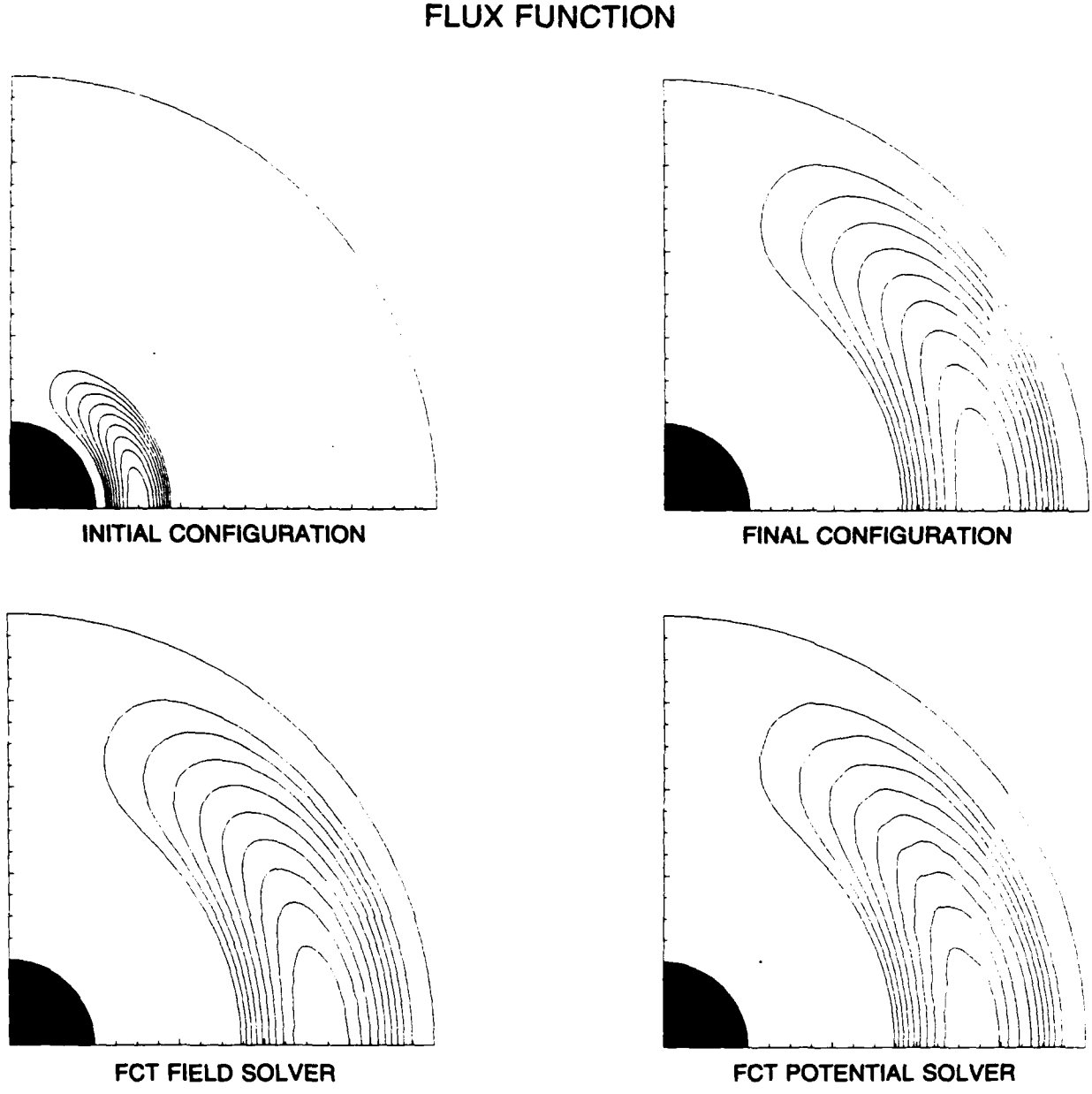

Figure 4. The flux function $\psi = r \sin\theta A_\phi$ for a self-similar spherical expansion of a magnetic bubble embedded in a stellar envelope is displayed, in its initial and exact final states (top) and in the final states produced by the FCT solvers (bottom). The domain $r_0 \leq r \leq 5r_0$, $0 \leq \theta \leq \frac{\pi}{2}$ is shown as projected against the sky; the shaded region is $r \leq r_0$. The flux function is contoured at 10%, 20%, ..., 90% of its peak initial value.

for $r_1 = 0.55\ r_0$ and $r_2 = 0.95\ r_0$. The simulations were carried out for times $2t_0 \leq t \leq 5t_0$, on the spatial grid $r_0 \leq r \leq 5r_0$, $0 \leq \theta \leq \pi/2$. The 600 timesteps used correspond to an average Courant number of about 0.25, and the grid spacing on the 100 x 100 mesh increased linearly with r and was uniform in θ. A predictor/corrector integration method was used to time-center the source

terms and achieve second–order accuracy in time. Finally, the gravitational parameter GMt_0^2/r_0^3 was assigned the special value 2/3, for which both the mass density and the pressure are continuous across the contact surface, and the flux constant ψ_0 was chosen to yield a minimum plasma β (ratio of plasma to magnetic pressure) of unity.

The flux surfaces at the initial and final times are shown in the upper panel of Fig. 4. Shown in the bottom panel are the solutions produced by the FCT field and potential solvers. They are quite similar, both qualitatively and quantitatively, although the field solver yields notably smoother flux surfaces. The errors in the flux function (8%) and the field components (20%) are essentially identical for the two solvers. As in the passive advection test, the potential solver yields the less accurate current density, by errors of 113% to 88%. Both solvers produce local current reversals in this problem, however — the potential solver at the 90% level and the field solver at the 10% level. Contour plots of the current densities are not shown because they are not very instructive. Numerically generated small–scale structures dominate the current distribution within the magnetic bubble.

Other numerical experiments have been carried out, and merit brief mention here. First, calculations performed with the bare low– and high–order schemes of the field solver exhibited much larger errors. In the *self–similar magnetic–bubble test*, for example, each scheme produced an error of about 60% in the flux function, compared to 8% when FCT is used to interpolate between them. Second, a planar magnetoacoustic shock propagated over a distance of 60 zones broadened from an initial two–zone discontinuity to a four–zone transition from pre– to post–shock conditions. The error in the magnetic field, evaluated over those four zones centered on the shock front, was less than 5% for the field solver. Third, the problem of the expansion of a cylinder of hot plasma against a uniform magnetic field, for which no analytic solution is known, was simulated for a 50:1 pressure ratio. In this test for monotonicity violations, the field solver produced undershoots and overshoots in the solution of only a few percent, despite the extreme conditions which prevailed early in the calculation. Finally, Evans and Hawley's [12] monotone upwind scheme for the hydromagnetic equation was applied to several of these problems. Their algorithm is not as accurate as the high–order scheme of the FCT solver, and consequently produced solutions with consistently larger errors, albeit with smoother (more diffuse) current profiles.

ACKNOWLEDGEMENTS

I benefitted significantly from insights and encouragement offered by both developers and users

of flux–corrected transport methods among my colleagues at the Naval Research Laboratory. Financial support was provided by the Office of Naval Research through the Naval Research Laboratory (JO 44-1527-0-7,8) and by the National Aeronautics and Space Administration (Solar Terrestrial Theory Program).

REFERENCES

1. J. P. Boris and D. L. Book, *J. Comput. Phys.* **11** (1973), 38.
2. D. L. Book, J. P. Boris, and K. Hain, *J. Comput. Phys.* **18** (1975), 248.
3. J. P. Boris and D. L. Book, *J. Comput. Phys.* **20** (1976), 397.
4. J. P. Boris, Flux–Corrected Transport Modules for Solving Generalized Continuity Equations, Naval Research Laboratory Report No. 3237, 1976.
5. S. T. Zalesak, *J. Comput. Phys.* **31** (1979), 335.
6. D. L. Book, J. P. Boris, and S. T. Zalesak, Flux–Corrected Transport, in "Finite–Difference Techniques for Vectorized Fluid Dynamics Calculations "(D. L. Book, ed.), Chap. 3, Springer–Verlag, New York, 1981.
7. R. H. Guirguis, Two–Dimensional Flux–Corrected Transport, JAYCOR Report No. J206–83–003/6201, March 1983.
8. G. Patnaik, R. H. Guirguis, J. P. Boris, and E. S. Oran, *J. Comput. Phys.* **71** (1987), 1.
9. R. Löhner, K. Morgan, M. Vahdati, J. P. Boris, and D. L. Book, *Comm. Appl. Num. Meth.* **4** (1988), 717.
10. C. R. DeVore, *J. Comput. Phys.* (1989), submitted.
11. D. Schnack and J. Killeen, *J. Comput. Phys.* **35** (1980), 110.
12. C. R. Evans and J. F. Hawley, *Astrophys. J.* **332** (1988), 659.
13. B. C. Low, *Astrophys. J.* **281** (1984), 381.
14. B. C. Low, *Astrophys. J.* **281** (1984), 392.